INTERNATIONAL JOURNAL FOR NUMERICAL METHODS IN FLUIDS
Int. J. Numer. Meth. Fluids 2011; **66**:1475–1494
Published online 6 April 2010 in Wiley Online Library (wileyonlinelibrary.com). DOI: 10.1002/fld.2321

A novel implicit numerical treatment for non-linear turbulence models using high and low Reynolds number formulations

Marcelo Assato and Marcelo J. S. de Lemos*, †

Departamento de Energia—IEME, Instituto Tecnológico de Aeronáutica—ITA, 12228-900 São José dos Campos, SP, Brazil

SUMMARY

Non-linear turbulence models can be seen as an improvement of the classical eddy-viscosity concept due to their better capacity to simulate characteristics of important flows. However, application of non-linear models demand robustness of the numerical method applied, requiring a stable discretization scheme for convergence of all variables involved. Usually, non-linear terms are handled in an explicit manner leading to possible numerical instabilities. Thus, the present work shows the steps taken to adapt a general non-linear constitutive equation using a *new semi-implicit* numerical treatment for the non-linear diffusion terms. The objective is to increase the degree of implicitness of the solution algorithm to enhance convergence characteristics. Flow over a backward-facing step was computed using the control volume method applied to a boundary-fitted coordinate system. The SIMPLE algorithm was used to relax the algebraic equations. Classical wall function and a low Reynolds number model were employed to describe the flow near the wall. The results showed that for certain combination of relaxation parameters, the semi-implicit treatment proposed here was the sole successful treatment in order to achieve solution convergence. Also, application of the implicit method described here shows that the stability of the solution either increases (high Reynolds with non-orthogonal mesh) or preserves the same (low Reynolds number applications). Additional advantages of the procedure proposed here lie in the possibility of testing different non-linear expressions if one considers the enhanced robustness and stability obtained for the entire numerical algorithm. Copyright © 2010 John Wiley & Sons, Ltd.

Received 20 June 2008; Revised 2 February 2010; Accepted 7 February 2010

KEY WORDS: turbulence modelling; non-linear models; control volume method

1. INTRODUCTION

It is well established in the literature that eddy-viscosity turbulence models (EVMs) do not, on the whole, cope well with strong streamline curvature whether it arises from flow over curved surfaces or imparted swirling [1]. Yet, turbulence-driven secondary motion and directional effects due to buoyancy cannot, due to the absence of information about individual stresses, be fully simulated with EVMs. In spite of that, they are often used in engineering computations due to the numerical robustness obtained via its linear *stress–strain rate* relationship [2]. This diffusion-like approach makes the numerical solution stable, with the model easily adaptable to existing computer code architectures. Another route to follow is the solution of transport equations for the individual

*Correspondence to: Marcelo J. S. de Lemos, Departamento de Energia—IEME, Instituto Tecnológico de Aeronáutica—ITA, 12228-900 São José dos Campos, SP, Brazil.
†E-mail: delemos@ita.br

Contract/grant sponsor: CNPq, Brazil

turbulent stresses. Such Reynolds Stress Models (RSMs), [3] are not based on a *turbulent stress–mean strain rate* relationship. Thus, the connection between *mean* and *turbulent* fields is somewhat 'loose' in the sense that turbulence is also associated with mechanisms of convection and diffusion, in its own transport equation set, rather than the simpler diffusion term plugged into the mean flow equation.

Models involving other types of constitutive equations have been lately developed with the perspective of applying Computational Fluid Dynamics (CFD) to complex flows. These techniques aim, at a wider range of applicability, similar to that of RSMs, while keeping computational costs down to EVM cost levels. Theories employing other type of representation of individual Reynolds stresses/fluxes, including addition of non-linear terms to the basic constitutive equation, try to capture the sensitivity to flow curvatures and buoyancy, a feature missing in basic EVMs.

Developments in this area can be roughly classified into two major groups. The first comes from the direct modelling of the Reynolds Averaged Navier–Stokes (RANS) equations with some approximation for the net transport of the stresses ([*Convection*]−[*Diffusion*]). In that, *algebraic*, instead of *transport* equations, are devised to predict individual stresses. These algebraic relations can be either of an *implicit* characteristic leading to the so-called Algebraic Stress Model (ASM), [4–6] or else, involve approximations yielding to an *explicit* expression for $-\rho\overline{u_i' u_j'}$ [7]. In both cases, the algebraic formulae are a direct consequence of the RANS equations.

The other major approach is usually of an *ad hoc* nature and basically follows the procedures used in obtaining constitutive equations for the laminar flow of non-Newtonian fluids [8]. An example is the work of Speziale [9]. Essentially, the observed relationship between the laminar flow of viscoelastic fluids and the turbulent flow of Newtonian substances has motivated developments in such direction [10]. The basic advantage of this approach over the former lies on the achieved computational savings when compared with ASMs (roughly 25–50% less computing time).

To the best of the authors' knowledge, most of the published work on non-linear models [9, 11–14] are either written for the Cartesian coordinates and/or treat additional non-linear terms in a fully explicit manner. The recent literature has recognized the difficulty in obtaining convergence when running non-linear models in complex flows. The work of Bauer *et al.* [15] concludes that the convergence is only obtained after a 'quasi-linear' truncation of non-linear terms. Further, Abid *et al.* [16] and Rahman *et al.* [17] also reported difficulties when applying the non-linear model of Gatski and Speziale [14]. Therefore, engineering applications of non-linear models can benefit from the development of numerical artifices to enhance solution stability and robustness. Ultimately, solving complex flows on non-orthogonal grids using advanced non-linear models is not an easy job. Frequently, calculations require severe under relaxation and the implementation of convergence acceleration schemes.

Based on this demand, this work presents the steps taken to adapt a non-linear model into a generalized coordinate system, where a *new* numerical treatment is proposed to handle a general non-linear constitutive equation into a boundary-fitted computer code. The numerical methodology proposed here contributes to the robustness of the solution method and increases the applicability of such non-linear models to numerical grids, fully complacent with irregular computational domains. In addition, two methods are used to describe the flow near the wall, namely the classical wall function approach and a low Reynolds number model. The results for backward-facing step problem are shown.

Here, transport equations are first presented followed by a description of non-linear models. Details of the numerical method employed are shown prior to the description of the implicit numerical procedure.

2. TRANSPORT EQUATIONS

In this work, the equations to follow are based on the use of statistical tools, like time-averaging, in order to obtain the so-called RANS equations. Thus, the general equations describing the flow

DOI: 10.1002/fld

Table I. Transport coefficients and source terms.

ϕ	k	ε
Γ_ϕ	$\frac{\mu_t}{\sigma_k}$	$\frac{\mu_t}{\sigma_\varepsilon}$
S_ϕ	$P_k-\rho\varepsilon$	$\frac{\varepsilon}{k}(c_1P_k-c_2f_2\rho\varepsilon)$
where $P_k=\tau_{ij}^t\frac{\partial U_i}{\partial x_j}$, $\mu_t=\rho c_\mu f_\mu\frac{k^2}{\varepsilon}$		

of fluids can be written in the following form:

$$\text{Mass: } \operatorname{div}(\rho\vec{v})=0, \tag{1}$$

$$\text{Momentum: } \operatorname{div}(\rho\vec{v}U_i-\vec{t}_i)=s_{u_i}. \tag{2}$$

Additional transport equation for scalar transport reads:

$$\text{Scalar: } \operatorname{div}(\rho\vec{v}\phi-\vec{q}_\phi)=s_\phi, \tag{3}$$

where $\vec{v}$ is the time-mean velocity vector, $\vec{t}_i$ in Equation (2) contains the stresses acting in the i-direction and s_{u_i} represents all source terms given by:

$$\vec{t}_i=\tau_{ij}\cdot\vec{i}_j, \tag{4}$$

$$s_{u_i}=-\frac{\partial P}{\partial x_i}, \quad P=p+\rho gh+\frac{2}{3}\rho k. \tag{5}$$

In Equation (3), ϕ represents a scalar quantity, $\vec{q}_\phi$ is its diffusive flux and s_ϕ the source or sink of ϕ. The two scalars of concern in this work are the turbulent kinetic energy k and its dissipation rate ε. The general expression for $\vec{q}_\phi$ is given as:

$$\vec{q}_\phi=\Gamma_\phi\operatorname{grad}\phi=\frac{\mu_t}{\sigma_\phi}\left(\frac{\partial\phi}{\partial y^j}\vec{i}_j\right), \tag{6}$$

where σ_ϕ is a constant and y^j are the Cartesian coordinates. The transport coefficient, Γ_ϕ, and the sources terms, s_ϕ, for the $k-\varepsilon$ equations are expressed in Table I. The symbols P_k and μ_t, in Table I, represent the turbulence kinetic energy production rate and the eddy viscosity, respectively.

The total pressure P in (5) also involves a term containing the turbulent kinetic energy $k=\overline{u_i'u_i'}/2$, where u_i' is the fluctuating part of the instantaneous velocity in the i-direction and h is the height in the definition of hydrostatic pressure. Although the use of (5) is not mandatory for the computation of pressure field with iterative processes, such proposition makes the stress–strain relationship much simpler, similar to that of handling Newtonian fluids in laminar flows. The stress, τ_{ij}, in Equation (4) represents the sum of the Reynolds stress, τ_{ij}^t, plus the viscous stress $\tau_{ij}^\ell=\mu S_{ij}$, where the deformation tensor is given by

$$S_{ij}=\left(\frac{\partial U_i}{\partial x_j}+\frac{\partial U_j}{\partial x_i}\right), \tag{7}$$

where U_i and U_i are the velocity components in the i and j directions, respectively. Different constitutive equations for τ_{ij}^t for turbulent flow will be discussed later and they shall be classified basically in **L**inear and **N**on-**L**inear relationships.

In the present work, both high and low Reynolds number models are compared with each other. High Reynolds number model is an approach that considers the use of wall functions for bypassing the viscous regions close to the walls. On the other hand, low Reynolds number models compute the flow within the viscous region. Their basic difference lies in the distinct form of the damping functions f_μ and f_2 which are referred in Table I and defined in Table II. These functions and a slightly different set of constants are used in conjunction with the k-ε equations. The two sets of

DOI: 10.1002/fld

Table II. Damping functions and constants for high and low Reynolds models.

	High Reynolds model proposed by Launder and Spalding [18]	Low Reynolds model proposed by Abe *et al.* [19]
f_μ	1.0	$\left\{1-\exp\left[-\frac{(\nu\varepsilon)^{0.25}n}{14\nu}\right]\right\}^2\left\{1+\frac{5}{(k^2/\nu\varepsilon)^{0.75}}\exp\left[-\left(\frac{(k^2/\nu\varepsilon)}{200}\right)^2\right]\right\}$
f_2	1.0	$\left\{1-\exp\left[-\frac{(\nu\varepsilon)^{0.25}n}{3.1\nu}\right]\right\}^2\left\{1-0.3\exp\left[-\left(\frac{(k^2/\nu\varepsilon)}{6.5}\right)^2\right]\right\}$
σ_k	1.0	1.4
σ_ε	1.33	1.3
c_1	1.44	1.5
c_2	1.92	1.9
τ_w	$\frac{u_P\rho c_\mu^{\frac{1}{4}}\kappa k_P^{\frac{1}{2}}}{\ln\left(\frac{E\rho c_\mu^{\frac{1}{4}}k_P^{\frac{1}{2}}y_P}{\mu}\right)}$	$\mu\frac{\partial u}{\partial y}$

constants employed here are also presented in Table II and encompass the two forms of turbulence models considered here.

While calculating the wall shear stress with the high Reynolds method [18], E, a parameter shown in Table II, may vary to simulate the surface roughness. Also, in Table II the von Kármán constant has the value $\kappa=0.41$. Subscript P refers to the node next to the wall. Thus u_P and k_P are, respectively, the value of the velocity and turbulent kinetic energy in this point, and y_P is the normal distance to the wall. The symbol n in the low Reynolds number model represents the normal coordinate to the wall.

3. NON-LINEAR EDDY-VISCOSITY MODELS

The so-called Boussinesq approximation for the linear stress–strain rate relationship is written in its general form as

$$\tau_{ij}^t=\mu_t S_{ij}+\tfrac{2}{3}\rho\delta_{ij}k. \tag{8}$$

As mentioned before, the last term in (8) was compacted into an expression for the total pressure P given in Equation (5). Here, the advantages in the composition of P in (5) is seen, since a much simpler stress–strain relationship is obtained not only for the laminar flow but also for turbulent regime.

Non-linear eddy-viscosity models originated in a general proposal was done by Pope [20]. However, only in the past two decades such models had greater progress, particularly with the works of Speziale [9], Nisizima and Yoshizawa [11], Rubinstein and Barton [12], Shih *et al.* [13], among others. In these works, quadratic products were introduced involving the strain and vorticity tensors with different derivations and calibrations for each model. These quadratic forms produce a certain anisotropy degree among the normal tensions, which make possible to predict, among other processes, the presence of secondary motion in non-circular ducts.

A general non-linear expression for the Reynolds stress, kept to second order, can be written as:

$$\begin{aligned}\tau_{ij}^t=&-(\mu_t S_{ij})^{\mathrm{L}}+\left(c_{1\mathrm{NL}}\mu_t\frac{k}{\varepsilon}\left[S_{im}S_{mj}-\frac{1}{3}S_{ml}S_{ml}\delta_{ij}\right]\right)^{\mathrm{NL1}}\\&+\left(c_{2\mathrm{NL}}\mu_t\frac{k}{\varepsilon}[\Omega_{im}S_{mj}+\Omega_{jm}S_{mi}]\right)^{\mathrm{NL2}}+\left(c_{3\mathrm{NL}}\mu_t\frac{k}{\varepsilon}\left[\Omega_{im}\Omega_{jm}-\frac{1}{3}\Omega_{lm}\Omega_{lm}\delta_{ij}\right]\right)^{\mathrm{NL3}},\end{aligned} \tag{9}$$

$$\tau_{ij}^t=\tau_{ij}^{\mathrm{L}}+\tau_{ij}^{\mathrm{NL1}}+\tau_{ij}^{\mathrm{NL2}}+\tau_{ij}^{\mathrm{NL3}}, \tag{10}$$

DOI: 10.1002/fld

Table III. Constants and expressions for non-linear turbulence models.

Models	c_μ	$c_{1\mathrm{NL}}$	$c_{2\mathrm{NL}}$	$c_{3\mathrm{NL}}$	Extra term
Nisizima and Yoshizawa [11]	0.09	−0.76	0.18	1.04	T_{SPE}
Speziale [9]	0.09	−0.1512	0.0	0.0	
Rubinstein and Barton [12]	0.0845	0.68	0.14	−0.56	
Shih *et al.* [13]	$\frac{2/3}{1.25+s+0.9\Omega}$	$\frac{0.75}{c_\mu(1000+s^3)}$	$\frac{3.8}{c_\mu(1000+s^3)}$	$\frac{4.8}{c_\mu(1000+s^3)}$	
Park and Sung [21]	0.09	0.6	0.4	0.005	

$T_{\mathrm{SPE}}=-0.3024\mu_t k/\varepsilon\{\tilde{S}_{ij}-\frac{1}{3}\tilde{S}_{mm}\delta_{ij}\}$, where $\tilde{S}_{ij}=\frac{\partial S_{ij}}{\partial t}+\vec{V}\cdot S_{ij}-\frac{\partial V_i}{\partial x_k}S_{kj}-\frac{\partial V_j}{\partial x_k}S_{ki}$, $s=\frac{k}{\varepsilon}\sqrt{\frac{1}{2}S_{ij}S_{ij}}$, $\Omega=\frac{k}{\varepsilon}\sqrt{\frac{1}{2}\Omega_{ij}\Omega_{ij}}$.

where δ_{ij} is the delta Kronecker; the superscripts in Equation (9) indicate **L**inear and **N**on-**L**inear contributions, S_{ij} is the deformation tensor given by (7) and Ω_{ij} represents the vorticity tensor written as:

$$\Omega_{ij}=\left(\frac{\partial U_i}{\partial x_j}-\frac{\partial U_j}{\partial x_i}\right). \tag{11}$$

Equations (9) and (10) already assume that the term $2/3\rho\delta_{ij}k$ is combined into the total pressure P shown in (5). The different values of c_μ, $c_{1\mathrm{NL}}$, $c_{2\mathrm{NL}}$ and $c_{3\mathrm{NL}}$, proposed in the literature are shown in Table III. In most of the models their values remain constant, except in the model proposed by Shih *et al.* [13], where they vary spatially within the flow. The theory of Speziale [9], has an origin different from the others. In his development, Speziale [9], based his model on a similarity between the mean turbulent flow of a Newtonian fluid and the laminar flow of a viscoelastic fluid.

Combining the quadratic terms in Equation (9), one has further:

$$(\tau_{ij})^{\mathrm{NL1}}=c_{1\mathrm{NL}}\mu_t\frac{k}{\varepsilon}\left[A_{ij}+B_{ij}+C_{ij}+D_{ij}-\frac{1}{3}\delta_{ij}E_{lm}\right], \tag{12}$$

$$(\tau_{ij})^{\mathrm{NL2}}=2c_{2\mathrm{NL}}\mu_t\frac{k}{\varepsilon}[B_{ij}-C_{ij}], \tag{13}$$

$$(\tau_{ij})^{\mathrm{NL3}}=c_{3\mathrm{NL}}\mu_t\frac{k}{\varepsilon}\left[-A_{ij}+B_{ij}+C_{ij}-D_{ij}-\frac{1}{3}\delta_{ij}F_{lm}\right], \tag{14}$$

which, expanded in their general two-dimensional form ($l=1,2$ and $m=1,2$), becomes,

$$\begin{aligned}
A_{ij}&=\frac{\partial U_i}{\partial x_m}\frac{\partial U_m}{\partial x_j}\quad\text{or}\quad A_{ij}=\frac{\partial U_i}{\partial x_1}\frac{\partial U_1}{\partial x_j}+\frac{\partial U_i}{\partial x_2}\frac{\partial U_2}{\partial x_j}\quad\text{for } m=1,2,\\
B_{ij}&=\frac{\partial U_i}{\partial x_m}\frac{\partial U_j}{\partial x_m}\quad\text{or}\quad B_{ij}=\frac{\partial U_i}{\partial x_1}\frac{\partial U_j}{\partial x_1}+\frac{\partial U_i}{\partial x_2}\frac{\partial U_j}{\partial x_2}\quad\text{for } m=1,2,\\
C_{ij}&=\frac{\partial U_m}{\partial x_i}\frac{\partial U_m}{\partial x_j}\quad\text{or}\quad C_{ij}=\frac{\partial U_1}{\partial x_i}\frac{\partial U_1}{\partial x_j}+\frac{\partial U_2}{\partial x_i}\frac{\partial U_2}{\partial x_j}\quad\text{for } m=1,2,\\
D_{ij}&=\frac{\partial U_m}{\partial x_i}\frac{\partial U_j}{\partial x_m}\quad\text{or}\quad D_{ij}=\frac{\partial U_1}{\partial x_i}\frac{\partial U_j}{\partial x_1}+\frac{\partial U_2}{\partial x_i}\frac{\partial U_j}{\partial x_2}\quad\text{for } m=1,2,\\
E_{ml}&=\left(\frac{\partial U_m}{\partial x_l}+\frac{\partial U_l}{\partial x_m}\right)^2\quad\text{or}\quad E_{ml}=4\left(\frac{\partial U_1}{\partial x_1}\right)^2+4\left(\frac{\partial U_2}{\partial x_2}\right)^2+2\left(\frac{\partial U_1}{\partial x_2}+\frac{\partial U_2}{\partial x_1}\right)^2\\
&\qquad\text{for } l=1,2 \text{ and } m=1,2,\\
F_{lm}&=\left(\frac{\partial U_m}{\partial x_l}-\frac{\partial U_l}{\partial x_m}\right)^2\quad\text{or}\quad F_{ij}=2\left(\frac{\partial U_1}{\partial x_2}-\frac{\partial U_2}{\partial x_1}\right)^2\quad\text{for } l=1,2\quad\text{and}\quad m=1,2.
\end{aligned} \tag{15}$$

DOI: 10.1002/fld

Note that in Equation (7) U_i and U_i are the instantaneous velocity components in the general i and j directions, respectively, whereas in Equation (15) is considered only the time-averaged two-dimensional flows characterized by the Cartesian x (or 1) and y (or 2) components.

The development to follow is restricted to two dimensions because the testing cases presented are all relative to two-dimensional flows. In fact, for didactic purposes, the use of simpler two-dimensional derivations make it easier to convey to readers the ideas embodied in the novel numerical treatment presented here. Extension to full 3D discretization is naturally possible, but such development is not the objective of the present contribution. Turbulence is a recognized transient three-dimensional phenomenon, but here it is simulated with statistical tools and with the consideration of a two-dimensional geometry only. Thus, the flows considered below are those in which variables do not substantially vary in the third direction relatively to their variation along the first two coordinate axes.

4. NUMERICAL METHOD

4.1. Grid notation and transformation of coordinates

The numerical method employed for discretizing the governing equations is the control volume approach with a collocated grid. Figure 1 shows a typical control volume with the detailed notation, including the distances and indexing used when transforming the original equations into the $\eta-\xi$ coordinate system. The discretization methodology presented here has also been used in a previous work and has proved to be highly stable and robust [22].

For the sake of clarity and completeness, the derivations to follow are kept in the running text, instead of in the appendices, as in essence, they are the key information in the paper. Further, although the Finite volume method is a well-known and documented method, in most textbooks it is

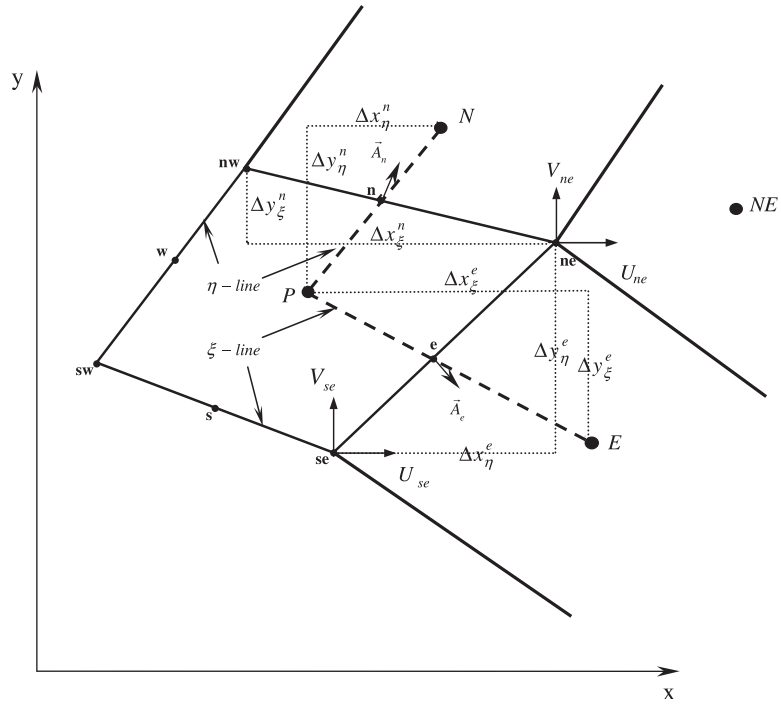

Figure 1. Control volume and notation.

DOI: 10.1002/fld

presented for orthogonal coordinate systems, which differs from the coordinate system considered here. Thus, with the help of Figure 1, the following operators can be identified:

$$\Delta x_\eta^e=(x_{ne}-x_{se}),\quad \Delta x_\xi^e=(x_E-x_P),\quad \Delta y_\eta^e=(y_{ne}-y_{se}),\quad \Delta y_\xi^e=(y_E-y_P), \tag{16}$$

$$\Delta x_\xi^n=(x_{ne}-x_{nw}),\quad \Delta x_\eta^n=(x_N-x_P),\quad \Delta y_\xi^n=(y_{ne}-y_{nw}),\quad \Delta y_\eta^n=(y_N-x_P). \tag{17}$$

The vector form of the area of the control volume at *east* and *north* faces, respectively, are given by:

$$\vec{A}_e=\Delta y_\eta^e\vec{i}-\Delta x_\eta^e\vec{j},\quad \vec{A}_n=-\Delta y_\xi^n\vec{i}+\Delta x_\xi^n\vec{j}. \tag{18}$$

The velocity derivatives and cross derivatives with respect to x and y appearing in Equations (9) and (11) can be expressed in terms of curvilinear coordinates in the following way:

$$\begin{aligned}\frac{\partial U}{\partial x}&=\frac{\partial\xi}{\partial x}\frac{\partial U}{\partial\xi}+\frac{\partial\eta}{\partial x}\frac{\partial U}{\partial\eta}=\frac{1}{J}\left[\frac{\partial y}{\partial\eta}\frac{\partial U}{\partial\xi}-\frac{\partial y}{\partial\xi}\frac{\partial U}{\partial\eta}\right],\\ \frac{\partial U}{\partial y}&=\frac{\partial\eta}{\partial y}\frac{\partial U}{\partial\eta}+\frac{\partial\xi}{\partial y}\frac{\partial U}{\partial\xi}=\frac{1}{J}\left[\frac{\partial x}{\partial\xi}\frac{\partial U}{\partial\eta}-\frac{\partial x}{\partial\eta}\frac{\partial U}{\partial\xi}\right],\end{aligned} \tag{19}$$

where J is the Jacobian of the transformation $(x, y)=f(\xi,\eta)$, defined as:

$$J=\frac{\partial x}{\partial\xi}\frac{\partial y}{\partial\eta}-\frac{\partial x}{\partial\eta}\frac{\partial y}{\partial\xi}. \tag{20}$$

In order to obtain the discrete forms of the governing equations, both the velocity derivatives and the Jacobian have to be approximated at faces of the control volume of Figure 1. For face 'e', derivatives of a general dependent variable φ can be approximated as:

$$\left(\frac{\partial\varphi}{\partial\xi}\right)_e\approx\frac{\varphi_E-\varphi_P}{\xi_E-\xi_P};\quad \left(\frac{\partial\varphi}{\partial\eta}\right)_e\approx\frac{\varphi_{ne}-\varphi_{se}}{\eta_{ne}-\eta_{se}}. \tag{21}$$

Here, for ease of notation, the following parameters are introduced based on the distances shown in Figure 1 for east face 'e':

$$\Pi_e=\Delta y_\eta^e\Delta x_\xi^e-\Delta y_\xi^e\Delta x_\eta^e;$$

$$\Delta U_\xi^e=(U_E-U_P);\quad \Delta U_\eta^e=(U_{ne}-U_{se}). \tag{22}$$

$$\Delta V_\xi^e=(V_E-V_P);\quad \Delta V_\eta^e=(V_{ne}-V_{se}). \tag{23}$$

$$\begin{aligned}\pi_a^e&=\Delta y_\eta^e(U_E-U_P)-\Delta y_\xi^e(U_{ne}-U_{se})=\Delta y_\eta^e\Delta U_\xi^e-\Delta y_\xi^e\Delta U_\eta^e;\\ \pi_b^e&=\Delta x_\xi^e(U_{ne}-U_{se})-\Delta x_\eta^e(U_E-U_P)=\Delta x_\xi^e\Delta U_\eta^e-\Delta x_\eta^e\Delta U_\xi^e;\\ \pi_c^e&=\Delta y_\eta^e(V_E-V_P)-\Delta y_\xi^e(V_{ne}-V_{se})=\Delta y_\eta^e\Delta V_\xi^e-\Delta y_\xi^e\Delta V_\eta^e;\\ \pi_d^e&=\Delta x_\xi^e(V_{ne}-V_{se})-\Delta x_\eta^e(V_E-V_P)=\Delta x_\xi^e\Delta V_\eta^e-\Delta x_\eta^e\Delta V_\xi^e.\end{aligned} \tag{24}$$

Similar expressions hold for the north face 'n'. Using (24) to represent (20) at the east face, one has:

$$J_e=\frac{\Delta y_\eta^e\Delta x_\xi^e-\Delta y_\xi^e\Delta x_\eta^e}{(\xi_E-\xi_P)(\eta_{ne}-\eta_{se})}=\frac{\Pi_e}{(\xi_E-\xi_P)(\eta_{ne}-\eta_{se})}, \tag{25}$$

yielding for Equation (19) at face 'e':

$$\begin{aligned}\left.\frac{\partial U}{\partial x}\right|_e&\approx\frac{(y_{ne}-y_{se})(U_E-U_P)-(y_E-y_P)(U_{ne}-U_{se})}{(x_E-x_P)(y_{ne}-y_{se})-(x_{ne}-x_{se})(y_E-y_P)}=\frac{\pi_a^e}{\Pi_e},\\ \left.\frac{\partial U}{\partial y}\right|_e&\approx\frac{(x_E-x_P)(U_{ne}-U_{se})-(x_{ne}-x_{se})(U_E-U_P)}{(x_E-x_P)(y_{ne}-y_{se})-(x_{ne}-x_{se})(y_E-y_P)}=\frac{\pi_b^e}{\Pi_e},\end{aligned} \tag{26}$$

DOI: 10.1002/fld

$$\left.\frac{\partial V}{\partial x}\right|_e \approx \frac{(y_{ne}-y_{se})(V_E-V_P)-(y_E-y_P)(V_{ne}-V_{se})}{(x_E-x_P)(y_{ne}-y_{se})-(x_{ne}-x_{se})(y_E-y_P)}=\frac{\pi_c^e}{\Pi_e},$$
$$\left.\frac{\partial V}{\partial y}\right|_e \approx \frac{(x_E-x_P)(V_{ne}-V_{se})-(x_{ne}-x_{se})(V_E-V_P)}{(x_E-x_P)(y_{ne}-y_{se})-(x_{ne}-x_{se})(y_E-y_P)}=\frac{\pi_d^e}{\Pi_e}. \tag{27}$$

4.2. Governing equations

For a general dependent variable φ, in a steady state flow, a discrete form of Equations (1)–(3) can be written as:

$$I_e+I_w+I_n+I_s=S_\varphi, \tag{28}$$

where I_e, I_w, I_n, I_s are the overall fluxes (convection plus diffusion) of φ at the *east*, *west*, *north* and *south* control volume faces, respectively, and S_φ the corresponding source term.

For the east face the total flux can be written for a general variable $\vec{\varphi}$ as:

$$I_e=\int_{A_e}(\vec{n}\cdot\vec{\varphi})\,\mathrm{d}A\approx(\vec{n}_e\cdot\vec{\varphi}_e)A_e, \tag{29}$$

where A_e is the control volume east face area, $\vec{n}_e$ is the unit vector normal to A_e and $\vec{\varphi}_e$ is the average value of $\vec{\varphi}$ prevailing over A_e. Also, for coherence in the discretization process, the continuity of fluxes at any interface implies that:

$$(I_w)_P=-(I_e)_W, \quad (I_s)_P=-(I_n)_S. \tag{30}$$

The numerical treatment of convection and diffusion mechanisms is handled separately. When Equation (28) is written for the x-direction, the convective flux, I^{C_x}, has contributions from both faces *east* 'e' and *north* 'n' in the following way:

$$I_e^{C_x}\approx F_eU_e, \quad I_n^{C_x}\approx F_nU_n, \tag{31}$$

where

$$F_e=\rho[U_e\Delta y_\eta^e-V_e\Delta x_\eta^e],$$
$$F_n=\rho[V_n\Delta x_\xi^n-U_n\Delta y_\xi^n]. \tag{32}$$

The flux-blended deferred correction scheme [23], indicated here as DCS, is employed to perform nodal interpolation. In this scheme, interface quantities are approximated as linear combination of central differencing scheme (CDS) and upwind differencing scheme (UDS) values [24] according to

$$\phi_{\text{face}}^{\text{DCS}}=\lambda\phi_{\text{face}}^{\text{CDS}}+(1-\lambda)\phi_{\text{face}}^{\text{UDS}}=\phi_{\text{face}}^{\text{UDS}}+\lambda(\phi_{\text{face}}^{\text{CDS}}-\phi_{\text{face}}^{\text{UDS}})^\circ, \tag{33}$$

where the quantities with superscript '°' in parenthesis (last equality) are the numerical values from the previous iteration. The combination factor λ may vary from 0 (pure UDS) to 1 (pure CDS). One should emphasize that the objective of this work was neither to investigate the use of high-order discretization schemes, nor to determine an optimal value for λ, but rather to propose a new implicit scheme to enhance the stability, and not the accuracy of the solution. Although it is recognized that the accuracy is always important, or say, the numerical solution should always provide reliable, physically realistic numbers that satisfy the original differential equation set, one can always increase the grid size to minimize the possible low-order effects resulting from the low-order discretization scheme. Nevertheless, one should mention that the use of (33) makes the resulting coefficient matrix positive with diagonal dominance, a factor that enhances stability [23].

For the diffusive flux in the same x-direction, I^{D_x}, both faces are also considered:

$$I_e^{D_x}\approx-(\tau_{11}\vec{i}+\tau_{12}\vec{j})_e\cdot\vec{A}_e, \tag{34}$$

$$I_n^{D_x}\approx-(\tau_{11}\vec{i}+\tau_{12}\vec{j})_n\cdot\vec{A}_n. \tag{35}$$

DOI: 10.1002/fld

Here, in accordance with Equation (10), the diffusion flux in each face for each direction can be split into *linear* and *non-linear* parts as:

$$I_e^{D_x} = -(\tau_{11}\vec{i}+\tau_{12}\vec{j})_e^{\mathrm{L}}\cdot\vec{A}_e-(\tau_{11}\vec{i}+\tau_{12}\vec{j})_e^{\mathrm{NL1}}\cdot\vec{A}_e \\ -(\tau_{11}\vec{i}+\tau_{12}\vec{j})_e^{\mathrm{NL2}}\cdot\vec{A}_e-(\tau_{11}\vec{i}+\tau_{12}\vec{j})_e^{\mathrm{NL3}}\cdot\vec{A}_e, \tag{36}$$

or

$$I_e^{D_x} = (I_e^{D_x})^{\mathrm{L}}+(I_e^{D_x})^{\mathrm{NL1}}+(I_e^{D_x})^{\mathrm{NL2}}+(I_e^{D_x})^{\mathrm{NL3}}. \tag{37}$$

Likewise, for the north face:

$$I_n^{D_x} = (I_n^{D_x})^{\mathrm{L}}+(I_n^{D_x})^{\mathrm{NL1}}+(I_n^{D_x})^{\mathrm{NL2}}+(I_n^{D_x})^{\mathrm{NL3}}. \tag{38}$$

Thus, a discrete form for (37) will be

$$(I_e^{D_x})^{\mathrm{L}} = -\frac{\mu_t^e}{\Pi_e}\{\Delta U_\xi^e[2(\Delta y_\eta^e)^2+(\Delta x_\eta^e)^2]-\Delta U_\eta^e[2\Delta y_\xi^e\Delta y_\eta^e+\Delta x_\xi^e\Delta x_\eta^e]-\pi_c^e\Delta x_\eta^e\}, \tag{39}$$

$$(I_e^{D_x})^{\mathrm{NL1}} = \frac{c_{1\mathrm{NL}}\mu_t^e k}{(\Pi_e)^2\varepsilon}\left\{-\Delta y_\eta^e\left[\frac{8}{3}(\pi_a^e)^2+\frac{1}{3}(\pi_b^e+\pi_c^e)^2-\frac{4}{3}(\pi_d^e)^2\right]+2\Delta x_\eta^e[(\pi_a^e+\pi_d^e)(\pi_b^e+\pi_c^e)]\right\}, \tag{40}$$

$$(I_e^{D_x})^{\mathrm{NL2}} = 2c_{2\mathrm{NL}}\frac{\mu_t^e}{(\Pi_e)^2}\frac{k}{\varepsilon}\{-\Delta y_\eta^e[(\pi_b^e)^2-(\pi_c^e)^2]+\Delta x_\eta^e[(\pi_d^e-\pi_a^e)(\pi_b^e-\pi_c^e)]\}, \tag{41}$$

$$(I_e^{D_x})^{\mathrm{NL3}} = c_{3\mathrm{NL}}\frac{\mu_t^e}{(\Pi_e)^2}\frac{k}{\varepsilon}\left\{-\Delta y_\eta^e\left[\frac{1}{3}(\pi_b^e-\pi_c^e)^2\right]\right\}, \tag{42}$$

where the velocity difference operators are defined by Equation (22).

At north face 'n' the diffusive fluxes have an analogous form. For the y-momentum equation, the diffusive fluxes at both east and north faces are also obtained in a similar fashion.

In the numerical treatment presented by Assato and de Lemos [25], as in the majority of similar non-linear calculations in the literature, the diffusion term is totally explicit in the sense that all terms in (38) are accommodated into the source term. In the present work, a different methodology is proposed as shown below.

4.3. Pressure source term

The source term due to integration of the pressure gradient over the control volume of Figure 1 gives for the x-direction:

$$S_{P_x} = -\left(\frac{\partial P}{\partial x}\right)\delta V, \tag{43}$$

where

$$\delta V = (y_n-y_s)(x_e-x_w)-(y_e-y_w)(x_n-x_s), \tag{44}$$

$$\frac{\partial P}{\partial x} \approx \frac{(P_e-P_w)(y_n-y_s)-(P_n-P_s)(y_e-y_w)}{(y_n-y_s)(x_e-x_w)-(y_e-y_w)(x_n-x_s)}. \tag{45}$$

Integration of (43) yields the following discrete form:

$$S_{P_x} \approx -(P_e-P_w)(y_n-y_s)+(P_n-P_s)(y_e-y_w). \tag{46}$$

Analogously, for the y-direction one has:

$$S_{P_y} \approx -(P_n-P_s)(x_e-x_w)+(P_e-P_w)(x_n-x_s). \tag{47}$$

DOI: 10.1002/fld

4.4. Treatment of equations for k and ε

The eddy-viscosity μ_t appearing in both Linear and Non-Linear parts of Equation (9) is calculated according to the equation shown in Table I. The function f_μ is presented in Table II, where E is a constant coming from the standard wall-log-law and n is the distance from the closest grid node to the wall. Governing equations for the non-linear $k-\varepsilon$ model are the same as for the linear model, except for differences in the Reynolds stresses expressions when calculating the production rate of k, P_k. The source terms for k and ε are given by

$$S_k = P_k - \rho\varepsilon; \quad S_\varepsilon = c_1 \frac{\varepsilon}{k}\left(P_k - \frac{c_2}{c_1}\rho\varepsilon\right), \tag{48}$$

where c_1 and c_2 are the constants also shown in Table II. Here, according to Equation (10), P_k in (48) is also split into a linear and a non-linear part in the form,

$$P_k = \tau_{ij}^t \frac{\partial U_i}{\partial y^j} = (\tau_{ij}^{\mathrm{L}} + \tau_{ij}^{\mathrm{NL1}} + \tau_{ij}^{\mathrm{NL2}} + \tau_{ij}^{\mathrm{NL3}}) \frac{\partial U_i}{\partial y^j} = P_k^{\mathrm{L}} + P_k^{\mathrm{NL1}} + P_k^{\mathrm{NL2}} + P_k^{\mathrm{NL3}}, \tag{49}$$

where τ_{ij}^t is given by Equation (9). As done for the pressure gradient term, integration of S_ϕ (Equation (48), $\phi = k, \varepsilon$) over the cell volume surrounding point P in Figure 1 gives [24],

$$\overline{S_\phi} \cong \int_{\delta V} S_\phi \delta V = S_\phi^* - S_\phi^{**}\phi_P. \tag{50}$$

The dependence on ϕ_P is sometimes artificially introduced when a negative part of S_ϕ does not exist [24]. After integrating S_k in the form of (50) one has:

$$S_k^* = (P_k^{\mathrm{L}} + P_k^{\mathrm{NL1}} + P_k^{\mathrm{NL2}} + P_k^{\mathrm{NL3}})\delta V; \quad -S_k^{**}k = -\rho\varepsilon\delta V = -\left(\frac{\rho\varepsilon^\circ \delta V}{k^\circ}\right)k. \tag{51}$$

Again, the values of k and ε with superscript '$\circ$' in (51) are taken from the previous iteration and, when the solution finally converges, $k^\circ \to k$ and the two values cancel out. For S_ε, the choices for S_ε^* and S_ε^{**} are $S_\varepsilon^* = c_1 \varepsilon S_k^*/k$; $S_\varepsilon^{**} = c_2 S_k^{**}$, respectively.

The production rate P_k needs to be evaluated at the central point P. To this end, derivatives of the mean velocities with respect to Cartesian coordinate directions are transformed similarly to expressions (26) and (27), but now written for central nodal points rather than for control volume faces, as,

$$\begin{aligned}
\left(\frac{\partial U}{\partial x}\right)_P &= \frac{(y_n - y_s)(U_e - U_w) - (y_e - y_w)(U_n - U_s)}{(y_n - y_s)(x_e - x_w) - (y_e - y_w)(x_n - x_s)} = \frac{\Delta y_\eta^P \cdot \Delta U_\xi^P - \Delta y_\xi^P \cdot \Delta U_\eta^P}{\Delta y_\eta^P \cdot \Delta x_\xi^P - \Delta y_\xi^P \cdot \Delta x_\eta^P} = \frac{\pi_a^P}{\Pi_P}, \\
\left(\frac{\partial U}{\partial y}\right)_P &= \frac{(U_n - U_s)(x_e - x_w) - (U_e - U_w)(x_n - x_s)}{(y_n - y_s)(x_e - x_w) - (y_e - y_w)(x_n - x_s)} = \frac{\Delta U_\eta^P \cdot \Delta x_\xi^P - \Delta U_\xi^P \cdot \Delta x_\eta^P}{\Delta y_\eta^P \cdot \Delta x_\xi^P - \Delta y_\xi^P \cdot \Delta x_\eta^P} = \frac{\pi_b^P}{\Pi_P},
\end{aligned} \tag{52}$$

$$\begin{aligned}
\left(\frac{\partial V}{\partial x}\right)_P &= \frac{(y_n - y_s)(V_e - V_w) - (y_e - y_w)(V_n - V_s)}{(y_n - y_s)(x_e - x_w) - (y_e - y_w)(x_n - x_s)} = \frac{\Delta y_\eta^P \cdot \Delta V_\xi^P - Deltay_\xi^P \cdot \Delta V_\eta^P}{\Delta y_\eta^P \cdot \Delta x_\xi^P - \Delta y_\xi^P \cdot \Delta x_\eta^P} = \frac{\pi_c^P}{\Pi_P}, \\
\left(\frac{\partial V}{\partial y}\right)_P &= \frac{(V_n - V_s)(x_e - x_w) - (V_e - V_w)(x_n - x_s)}{(y_n - y_s)(x_e - x_w) - (y_e - y_w)(x_n - x_s)} = \frac{\Delta V_\eta^P \cdot \Delta x_\xi^P - \Delta V_\xi^P \cdot \Delta x_\eta^P}{\Delta y_\eta^P \cdot \Delta x_\xi^P - \Delta y_\xi^P \cdot \Delta x_\eta^P} = \frac{\pi_d^P}{\Pi_P},
\end{aligned} \tag{53}$$

where the πs, as before, are used for ease of notation. With the expressions above, the linear part in Equation (49) then has the following discrete expression:

$$P_k^{\mathrm{L}} = \frac{\mu_t^P}{(\Pi_P)^2}[2(\pi_a^P)^2 + 2(\pi_b^P)^2 + (\pi_c^P + \pi_d^P)^2], \tag{54}$$

DOI: 10.1002/fld

and for the non-linear counterparts:

$$P_k^{\mathrm{NL1}} = -c_{1\mathrm{NL}} \frac{\mu_t^P}{(\Pi_P)^3} \frac{k}{\varepsilon} \left\{ \frac{8}{3}(\pi_a^P)^3 + \frac{8}{3}(\pi_b^P)^3 + \frac{7}{3}(\pi_a^P + \pi_b^P)[(\pi_c^P + \pi_d^P)^2 - \frac{4}{7}(\pi_c^P \cdot \pi_d^P)] \right\}, \tag{55}$$

$$P_k^{\mathrm{NL2}} = 0, \tag{56}$$

$$P_k^{\mathrm{NL3}} = -c_{3\mathrm{NL}} \frac{\mu_t^P}{(\Pi_P)^3} \frac{k}{\varepsilon} \left[\frac{1}{3}(\pi_a^P + \pi_b^P)(\pi_c^P - \pi_d^P)^2 \right]. \tag{57}$$

Values of the velocity components at cell face, as well as the coordinates of these locations, are calculated from the nodal values by means of linear interpolation.

5. NEW IMPLICIT TREATMENT

It is a well-known feature that increasing the degree of solution implicitness, the robustness of the relaxation process is enhanced [24]. Source-term linearization is a common procedure among the CFD practitioners and, in the end, intends to increase the main diagonal dominance of the matrix of coefficients. The work here aims at increasing the robustness of the numerical method without resorting to the techniques that simultaneously operate on more than one dependent variable, as is the case of block-implicit methods [1, 26, 27]. Here, implicit handling of individual momentum equations is considered. Accordingly, to improve numerical stability, the diffusive terms given by Equations (39)–(42) are further rewritten as a combination of *implicit* and *explicit* parts in the form,

$$(I_e^{D_x})^{\mathrm{L}} = -\Delta U_\xi^e (D_e^{x,y})^{\mathrm{L}} + (S_e^{*x})^{\mathrm{L}}, \tag{58}$$

$$(I_e^{D_x})^{\mathrm{NL1}} = \Delta U_\xi^e (D_e^{x,y})^{\mathrm{NL1}} + (S_e^{*x})^{\mathrm{NL1}}, \tag{59}$$

$$(I_e^{D_x})^{\mathrm{NL2}} = \Delta U_\xi^e (D_e^{x,y})^{\mathrm{NL2}} + (S_e^{*x})^{\mathrm{NL2}}, \tag{60}$$

$$(I_e^{D_x})^{\mathrm{NL3}} = \Delta U_\xi^e (D_e^{x,y})^{\mathrm{NL3}} + (S_e^{*x})^{\mathrm{NL3}}, \tag{61}$$

where the velocity difference operator, ΔU_ξ^e, is defined in (22). Equations (58)–(61) are written for the x-component diffusion flux of the *east* face of Figure 1 and basically represent the main idea of (50). Similar expressions can be written for all other faces and for the y-component of the diffusion flux. It is interesting to emphasize that even for a standard linear model, source term linearization given by (58) applies.

The first terms on the right-hand side of Equations (58)–(61) are the terms treated implicitly whereas the second terms are handled in an explicit manner. The coefficient $D_e^{x,y}$ is the same for both the equations in x and y components, and is given by

$$D_e^{x,y} = (D_e^{x,y})^{\mathrm{L}} + (D_e^{x,y})^{\mathrm{NL1}} + (D_e^{x,y})^{\mathrm{NL2}} + (D_e^{x,y})^{\mathrm{NL3}}, \tag{62}$$

where

$$(D_e^{x,y})^{\mathrm{L}} = \frac{(\mu + \mu_t^e)}{\Pi_e}[(\Delta y_\eta^e)^2 + (\Delta x_\eta^e)^2], \tag{63}$$

$$(D_e^{x,y})^{\mathrm{NL1}} = c_{1\mathrm{NL}} \frac{\mu_t^e}{(\Pi_e)^2} \frac{k}{\varepsilon} \left\{ -2(\Delta y_\eta^e)^2 \pi_a^e + 2\Delta x_\eta^e \left[\frac{4}{3} \Delta y_\eta^e (\pi_b^e + \pi_c^e) - \Delta x_\eta^e \pi_d^e \right] \right\}, \tag{64}$$

$$(D_e^{x,y})^{\mathrm{NL2}} = 2c_{2\mathrm{NL}} \frac{\mu_t^e}{(\Pi_e)^2} \frac{k}{\varepsilon} \{\Delta x_\eta^e \Delta y_\eta^e [\Delta x_\xi^e \Delta U_\eta^e - \Delta y_\xi^e \Delta V_\eta^e]\}, \tag{65}$$

$$(D_e^{x,y})^{\mathrm{NL3}} = c_{3\mathrm{NL}} \frac{\mu_t^e}{(\Pi_e)^2} \frac{k}{\varepsilon} \{\Delta x_\eta^e \Delta y_\eta^e [(\pi_b^e + \pi_c^e)]\}, \tag{66}$$

where ΔV_ξ^e and ΔV_η^e are given in (23).

DOI: 10.1002/fld

As mentioned before, by means of Equations (58)–(61), enhancement of matrix main diagonal dominance is achieved, contributing therefore towards the robustness of the entire numerical relaxation scheme.

The parts treating S_e^{*x} explicitly make use of velocity values at grid points calculated in the previous iteration. For the east face and x-direction one has:

$$(S_e^{*x})^{\mathrm{L}} = -\frac{(\mu+\mu_t)_e}{\Pi_e}\{(\Delta U_\xi^e)^\circ(\Delta y_\xi^e)^2 - (\Delta U_\eta^e)^\circ[2\Delta y_\xi^e \Delta y_\eta^e + \Delta x_\xi^e \Delta x_\eta^e] - \pi_c^e \Delta x_\eta^e\}, \tag{67}$$

$$\begin{aligned}(S_e^{*x})^{\mathrm{NL1}} = &-\frac{2c_{1\mathrm{NL}}\mu_t^e k}{(\Pi_e)^2\varepsilon}\left\{\Delta y_\eta^e\left[\frac{1}{3}(\pi_a^e)^2 + (\Delta U_\eta^e)^\circ\left(-\Delta y_\xi^e \pi_a^e + \Delta x_\xi^e\left(\frac{1}{3}\pi_c^e + \frac{1}{6}\Delta x_\xi^e (\Delta U_\eta^e)^\circ\right)\right)\right.\right.\\ &\left.-\frac{2}{3}(\pi_d^e)^2 + \frac{1}{6}(\pi_c^e)^2\right]\\ &-\Delta x_\eta^e\left[\frac{1}{6}\Delta x_\eta^e (\Delta U_\xi^e)^\circ \pi_a^e + (\Delta U_\eta^e)^\circ\left(\Delta x_\xi^e \pi_d^e - \Delta y_\xi^e\left(\pi_c^e + \frac{7}{6}\pi_b^e - \frac{1}{6}\Delta x_\xi^e (\Delta U_\eta^e)^\circ\right)\right)\right.\\ &\left.\left.+\pi_c^e \pi_d^e\right]\right\},\end{aligned} \tag{68}$$

$$\begin{aligned}(S_e^{*x})^{\mathrm{NL2}} = &-\frac{2c_{2\mathrm{NL}}\mu_t^e k}{(\Pi_e)^2\varepsilon}\{\Delta y_\eta^e[(\Delta x_\xi^e)^2((\Delta U_\eta^e)^\circ)^2 - (\pi_c^e)^2]\\ &-\Delta x_\eta^e[(\Delta y_\eta^e)^2(\Delta U_\xi^e)^\circ(\Delta V_\xi^e)^\circ + (\pi_b^e - \pi_c^e)(\Delta y_\xi^e(\Delta U_\eta^e)^\circ) + \pi_d^e]\},\end{aligned} \tag{69}$$

$$\begin{aligned}(S_e^{*x})^{\mathrm{NL3}} = \frac{c_{3\mathrm{NL}}\mu_t^e k}{(\Pi_e)^2\varepsilon}&\left\{-\frac{\Delta y_\eta^e}{3}[\Delta x_\eta^e(\pi_b^e + 3\pi_c^e - \Delta x_\eta^e(\Delta U_\xi^e)^\circ)(\Delta U_\xi^e)^\circ - 2\pi_b^e \pi_c^e + (\pi_c^e)^2\right.\\ &\left.+(\Delta x_\xi^e)^2((\Delta U_\eta^e)^\circ)^2]\right\}.\end{aligned} \tag{70}$$

Here, the decomposition of Equations (58)–(61) using coefficients (62)–(66) and explicit terms (67)–(70) represents a new proposal that, to the best of the authors' knowledge, is not found in the literature.

5.1. Final form of discretized momentum equation

After all fluxes and source terms are incorporated in the momentum equation, the algebraic equivalent of (2) is finally assembled. Variables at faces (e, w, n, s) and corners (ne, nw, se, sw) are interpolated forming an equation connecting the variable at P with its neighboring points (see Figure 1). Using expression (33) for interpolation the face values with UDS and CDS formulations, the final form can be written as,

$$\begin{aligned}a_P^{\mathrm{UDS}}\phi_P = \sum_{nb} a_{nb}^{\mathrm{UDS}}\phi_{nb} + S_\phi^* + \lambda\left(\sum_{nb} a_{nb}^{\mathrm{CDS}}\phi_{nb} - a_P^{\mathrm{UDS}}\phi_P\right)^\circ\\ \text{where } \phi = U, V \quad \text{and} \quad nb = E, W, N, S.\end{aligned} \tag{71}$$

Coefficients a_P and a_{nb} contain variables in the faces of the control volume obtained by interpolation of their respective nodal point values. For the east face, the coefficient reads,

$$a_E^{\mathrm{UDS}} = D_e^{x,y} + \|-F_e, 0\|, \tag{72}$$

$$a_E^{\mathrm{CDS}} = -\|-F_e, 0\| - F_e f_{x,P}, \tag{73}$$

DOI: 10.1002/fld

where the operator $\|A, B\|$ is greater between A and B, as in the FORTRAN language. Also, $D_e^{x,y}$ is calculated by means of (62) and F_e is given by (32) and f is an interpolation factor defined by (see Figure 1 for details),

$$f_{x,P} = \frac{x_e - x_P}{x_E - x_P}. \tag{74}$$

The source term S_U^* in the x-momentum equation can be assembled as:

$$S_U^* = \overbrace{S_e^{*x} - S_w^{*x} + S_n^{*x} - S_s^{*x}}^{\text{Explicit part of linear term}} + \underbrace{\overbrace{S_e^{*x} - S_w^{*x} + S_n^{*x} - S_s^{*x}}^{\text{Explicit part of 1st non-linear term}} + \overbrace{S_e^{*x} - S_w^{*x} + S_n^{*x} - S_s^{*x}}^{\text{Explicit part of 2nd non-linear term}} + \overbrace{S_e^{*x} - S_w^{*x} + S_n^{*x} - S_s^{*x}}^{\text{Explicit part of 3rd non-linear term}}}_{\text{These terms are null for standard linear models}} + \overbrace{S_{P_x}}^{\text{Pressure term}}, \tag{75}$$

where expressions similar to (67)–(70) are used at the four control volume faces and the pressure term is given by (46). The 5th to the 16th term in Equation (75) are null for standard linear models due to the fact that they are the result of the discretization of non-linear terms, which are presented in Equation (9).

The algorithm applied for solving the system of algebraic equations was the well-known pressure-based SIMPLE method by Patankar [24]. In such methods, linearization of the system of algebraic equations is handled by solving for each variable at a time while holding the other unknowns still.

6. RESULTS AND DISCUSSION

6.1. Preliminary discussion

Before presenting the numerical results, a discussion on the sensitivity of the discretized terms is essential. It is important to emphasize that coefficients $(D_e^{x,y})^{\mathrm{NL1}}$, $(D_e^{x,y})^{\mathrm{NL2}}$ and $(D_e^{x,y})^{\mathrm{NL3}}$, given by (64)–(66) respectively, have different numerical values on each control volume and depend on geometric distances, as well as on the surrounding velocity values. As such, they can be greater or less than zero. On the other hand, the linear coefficient given by (63), $(D_e^{x,y})^{\mathrm{L}}$, is composed of positive quantities only. Consequently, for *positive* non-linear coefficients $(D_e^{x,y})^{\mathrm{NL1}}$, $(D_e^{x,y})^{\mathrm{NL2}}$ and $(D_e^{x,y})^{\mathrm{NL3}}$, the advantages of the implicit treatment proposed here are not evident since numerical instabilities might occur during the relaxation process [24]. To make this idea clear, one remembers that the overall flux I, which was defined for each control volume face on the left-hand side of Equation (28), can be moved to the right-hand side for a source-like treatment. For the east face, it can be written in the form,

$$\overbrace{-(I_e^{D_x})^{\mathrm{L}}}^{\text{Source-like term}} = \underbrace{\Delta U_\xi^e}_{U_E - U_P} \overbrace{(D_e^{x,y})^{\mathrm{L}}}^{\text{always positive}} \underbrace{-(S_e^{*x})^{\mathrm{L}}}_{\text{Explicit term}}, \tag{76}$$

where $(D_e^{x,y})^{\mathrm{L}}$, as mentioned, is composed of positive quantities. Likewise, when (59) is accounted for as part of the diffusion term, as in Equation (37), and moved to the right of (28), one has,

$$-(I_e^{D_x})^{\mathrm{NL1}} = \underbrace{-\Delta U_\xi^e}_{U_P - U_E} \overbrace{(D_e^{x,y})^{\mathrm{NL1}}}^{\text{Less than '0' for stability}} \underbrace{-(S_e^{*x})^{\mathrm{NL1}}}_{\text{Explicit term}}, \tag{77}$$

DOI: 10.1002/fld

A similar argument can be used for expressions (60) and (61) involving $(D_e^{x,y})^{\mathrm{NL2}}$ and $(D_e^{x,y})^{\mathrm{NL3}}$, respectively.

Therefore, whenever *positive* values are detected in each control volume for $(D_e^{x,y})^{\mathrm{NL1}}$, the diffusive flux in question is handled back in an explicit form. In this case, Equation (59) is replaced by

$$(I_e^{D_x})^{\mathrm{NL1}} = -\Delta U_\xi^e \| - (D_e^{x,y})^{\mathrm{NL1}}, 0 \| + (\Delta U_\xi^e)^o \| (D_e^{x,y})^{\mathrm{NL1}}, 0 \| + (S_e^{*x})^{\mathrm{NL1}}, \tag{78}$$

Similar expressions hold for the second and third non-linear terms. With all the contributions due to diffusion properly accounted for in the Ds coefficients (see (62)), and applying expression (78) to the other non-linear diffusion coefficients $(D_e^{x,y})^{\mathrm{NL2}}$ and $(D_e^{x,y})^{\mathrm{NL3}}$, the coefficient a_E in Equation (72) is calculated.

The modifications above due to Equation (78) affect the way the velocity at the volume faces are calculated when applying the SIMPLE algorithm [28]. In this method, the basic idea is to solve a pressure correction equation derived from the momentum and continuity equations. It can be shown that the resulting pressure correction equation is [28],

$$a_P P'_P = a_W P'_P + a_E P'_P + a_S P'_P + a_N P'_P - S_m, \tag{79}$$

where the primes indicate corrections and S_m is known as the mass 'imbalance'. Face velocities, interpolated from values at main nodes, are used to compute S_m in (79). Therefore, the way the non-linear diffusion term is handled in (78) will influence computations of this mass source via the momentum equations. This influence, however, tends to decrease as the solution approaches convergence since both sides of (79) tend to zero. Also, it is important to emphasize that, for Cartesian grids or meshes with a high degree of orthogonality, the geometric distances Δx_η^e is null or nearly zero, respectively. This term appears in the formulae for the coefficients $(D_e^{x,y})^{\mathrm{NL1}}$, $(D_e^{x,y})^{\mathrm{NL2}}$ and $(D_e^{x,y})^{\mathrm{NL3}}$, Equations (64)–(66), respectively. If $\Delta x_\eta^e \approx 0$, only the first term in (64), if positive, will contribute to the main coefficient in (71). Therefore for an orthogonal or quasi-orthogonal grid, Equations (64)–(66) become,

$$(D_e^{x,y})^{\mathrm{NL1}} \approx c_{1\mathrm{NL}} \frac{\mu_t^e k}{(\Pi_e t)^2 \varepsilon} \left\{ -2(\Delta y_\eta^e)^2 \frac{\Delta U_\xi^e}{\Delta x_\xi^e} \right\}, \quad (D_e^{x,y})^{\mathrm{NL2}} \approx 0, \quad (D_e^{x,y})^{\mathrm{NL3}} \approx 0. \tag{80}$$

The solution method employed was the SIMPLE algorithm [28], as mentioned above. The algebraic equation systems, obtained after discretizing of the governing transport equations, were solved with an incomplete LU decomposition, known as Strongly Implicit Procedure [29]. This method has been tested in the developed code and applied to a number of geometries and flow configurations [30, 31].

6.2. Numerical results

The results presented in this section were obtained using four different models. The following turbulence closures were applied: the *linear* and *non-linear* $k-\varepsilon$ models combined with both the high and low Reynolds number approaches. Therefore, high Reynolds number models were designated by **L_HRN** and **NL_HRN**, for linear and non-linear closures, respectively, whereas low Reynolds models were named, respectively, by **L_LRN** and **NL_LRN**. For comparison, measurements of Kim *et al.* [32] were considered.

Results were obtained considering an inlet Reynolds number $Re = 132\,000$ based on the height of the step H together with inlet conditions for U, k and ε, according to Heyerichs and Pollard [33]. All boundary conditions are illustrated in Figure 2, where the symbol 'i' identifies the turbulence intensity of the incoming flow. The non-linear model employed was Shih *et al.* [13], closure. For high Reynolds model, orthogonal and non-orthogonal meshes of size 200×60 were used. For the low Reynolds number version, an orthogonal mesh of 227×100 was employed.

Table IV shows the separation length calculated by all four turbulence models. It can be noticed that smaller deviations are presented by the non-linear theory, with the best prediction obtained with the NL_LRN model.

DOI: 10.1002/fld

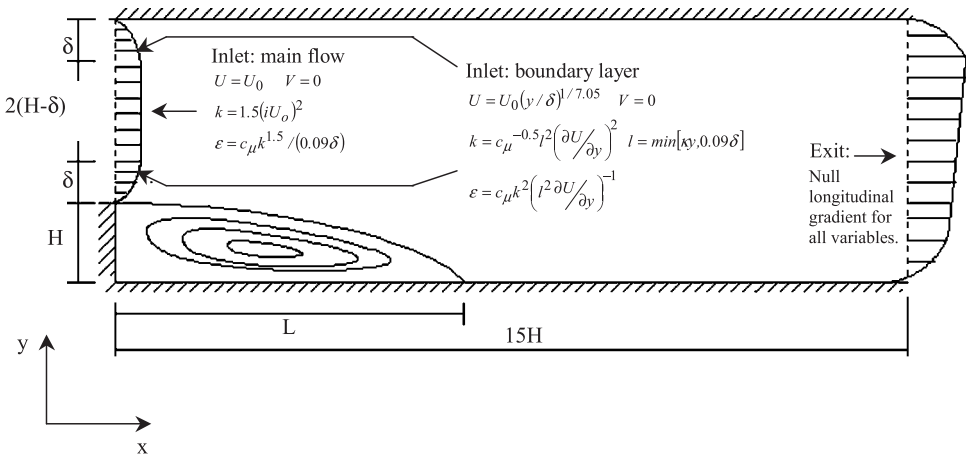

Figure 2. Boundary conditions for turbulent flow past a backward-facing step.

Table IV. Separation length x_R/H calculated with different models.

Models	Grid	Separation length: x_R/H	Deviations: % Experimental: $x_R/H = 7.0$
L_LRN	Orthogonal 227×100	5.65	19.29
NL_LRN	Orthogonal 227×100	6.55	6.43
L_HRN	Orthogonal 200×60	5.55	20.71
NL_HRN	Orthogonal 200×60	Expl.:6.45 Impl.andExpl.:6.45	7.86
L_HRN	Non-orthogonal 200×60	5.55	20.71
NL_HRN	Non-orthogonal 200×60	Expl.:6.45 Impl.andExpl.:6.45	7.86

Figure 3 shows the mean velocity field $\bar{U}/U_0$ in several stations along the channel. It can be seen that, in the recirculation region, better agreement for the mean velocity field occurs when the non-linear models are applied, with small advantage to the NL_LRN version. At $x/H = 8.0$ (after the reattachment section) the non-linear models predicted the worst results, with velocities lower than those measured experimentally.

Accordingly, for the turbulent flow past a backward-facing step it was verified that, in the recirculation zone, the non-linear models presented results for the mean velocity field which are closer to the experimental data (specially the NL_LRN model, see Figure 3). However, in the redeveloping zone, they showed a weak performance. Experiments by Kim *et al.* [32], show that in the section, right after the reattachment point, the velocity profiles do not follow the logarithmic law. Here, difficulties in the flow simulation were observed even with the low Reynolds number model. Results were better for axial positions far downstream from the reattachment point.

Figure 4(a),(b) shows better predictions for dimensionless turbulent intensity fields $(\overline{u'u'})^{1/2}$ and dimensionless turbulent shear stress $\overline{uv}$ when using non-linear models. It is interesting to observe that the NL_LRN closure is more accurate in the range $0.5 < Y/H < 0.8$, whereas improved results with the NL_HRN version occur only for $0.7 < Y/H < 1.0$.

In order to investigate the implicit numerical treatment proposed here and detect any contribution in the numerical stability of the solution, Figure 5 shows residue history for fictitious mass along the solution relaxation process using the NL_HRN model, which happens to be very similar to the residue history of component U (not shown here in this article). The figure compares both

DOI: 10.1002/fld

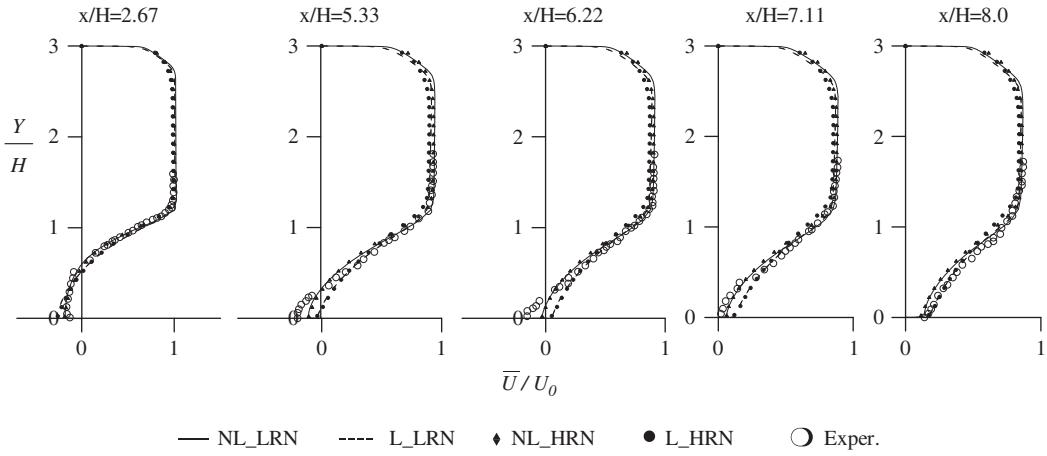

Figure 3. Dimensionless mean velocity profiles for the backward-facing step problem. Experiments by Kim *et al.* [32].

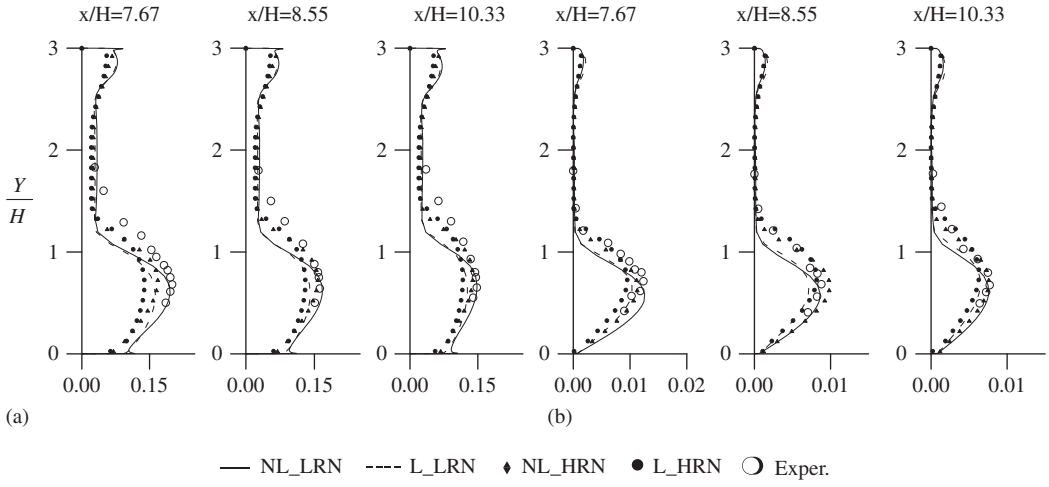

Figure 4. (a) Dimensionless turbulence intensities $\overline{u'u'}$ and (b) dimensionless turbulent shear stress, $\overline{u'v'}$. Experiments by Kim *et al.* [32].

semi-implicit and **fully explicit** formulations for discretizing the diffusion fluxes. Consequently, error-smoothing history is compared when discretization of the diffusion terms follows either (58)–(61) (*semi-implicit* or *explicit–implicit*) or a *fully explicit* formulation. Also presented is such behavior for two different grids, namely orthogonal and non-orthogonal meshes, which are presented in Figure 6. For the sake of clarity, not all nodes are presented in Figure 6. For both orthogonal and non-orthogonal cases, internal grid points are computed after the determination of boundary grid location, which are located according to the stretching functions applied along the boundaries. Incoming fluid from the left enters the computational domain by a gap of size given in Figure 5. Interior node coordinates are calculated by standard elliptical grid generation methods, in which partial differential equations are resolved once boundary node coordinates are known. Note that, for orthogonal grids, as expected, solution convergence is faster due to the absence of cross-derivatives in the discretized equation set. As may be seen by Equations (67)–(70), cross derivatives are handled explicitly, delaying convergence by increasing the stiffness of the algebraic equation system. In spite of difficulties due to grid type, no advantage with the semi-implicit formulation is noted if the relaxation parameters are low enough to decelerate the solution (sub-relax set A in Figure 5).

DOI: 10.1002/fld

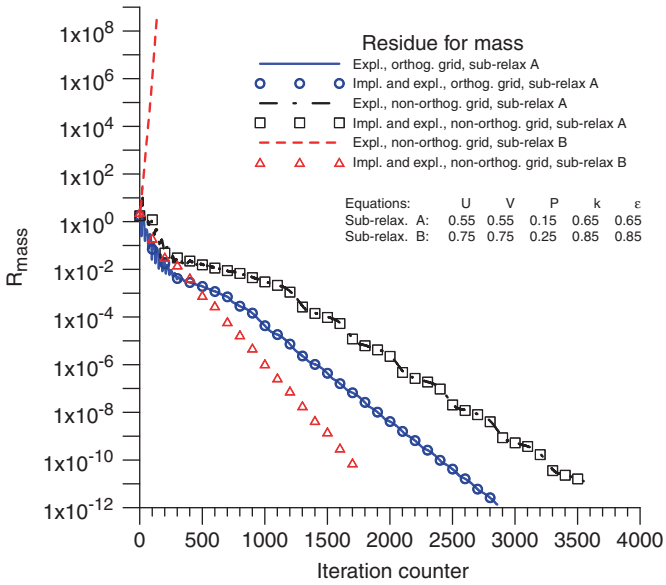

Figure 5. Residue history for fictitious mass for back-step case. Fully explicit and semi-implicit treatment using orthogonal and non-orthogonal grids of Figure 6. High Reynolds formulation with model of Shih *et al.* [13].

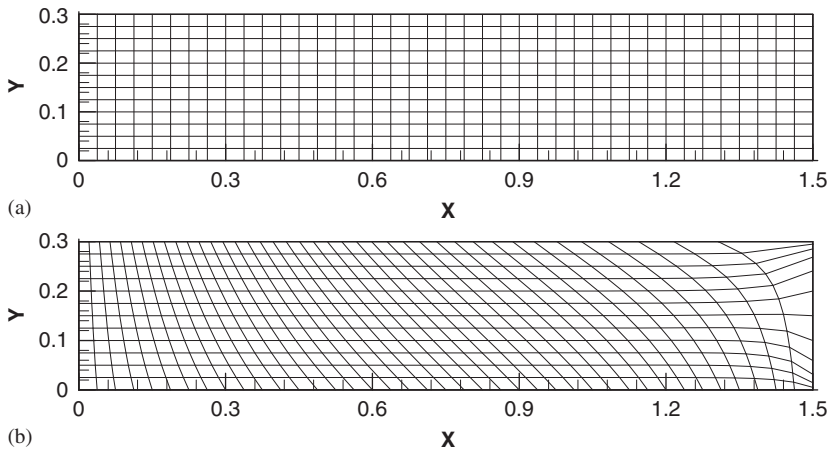

Figure 6. Orthogonal (a) and non-orthogonal grids (200×60) (b) used on high Reynolds residue history of Figure 5. Case back-step (not all points are shown for clarity).

In order to further investigate the advantages in using the proposed semi-implicit formulation, different relaxation factors for all the variables involved, namely, U, V, P, k and ε also were computed. Figure 5 also indicates that when the relaxation parameter is increased (sub-relax set B), even for a non-orthogonal mesh convergence is obtained, whereas with the fully explicit formulation, divergence is clearly observed.

Figure 7 further indicates the benefit of the numerical formulation proposed here when discretizing non-linear fluxes with the use of wall functions (high Reynolds approach). The model of Craft *et al.* [34], with constant coefficients $c_{1\mathrm{NL}}$, $c_{2\mathrm{NL}}$ and $c_{3\mathrm{NL}}$ is used and, regardless of the values of the relaxation parameters used, convergence is obtained only with the implementation proposed by Equations (58)–(61). The use of a low Reynolds number model in conjunction with a non-linear model has also been investigated here (see Table IV) and in other works [35, 36] leading to similar conclusions about the advantages in using the proposed implicit scheme. For such low

DOI: 10.1002/fld

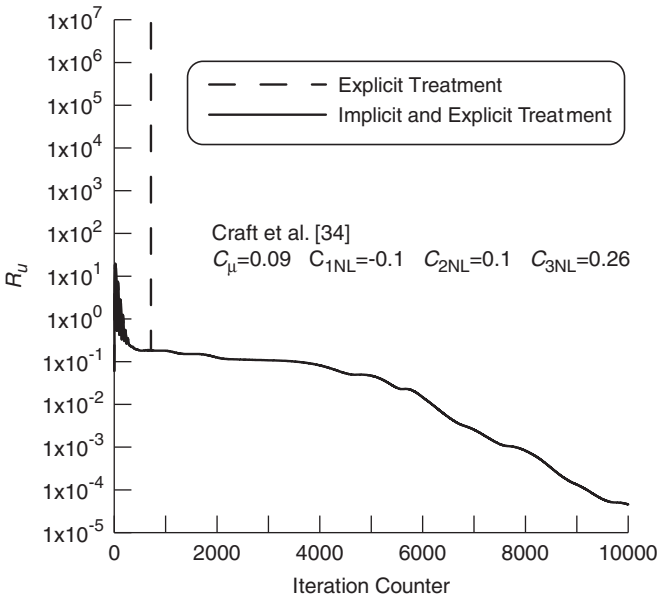

Figure 7. Residue for velocity component U. Case back-step. *Fully explicit* versus *semi-implicit* treatment for high Reynolds case and Craft *et al.* [34] model.

Reynolds number closure, both semi-implicit and fully explicit formulations presented the same convergence rate, independently whether the mesh was orthogonal or not and if a different set of relaxation values was used.

Finally, testing calculations herein showed that implicit handling of diffusion terms consumes only about 10% more computing time for the cases where solution is obtained with low relaxation parameters (note that the results in Figure 5 are plotted in terms of number of iterations, not computing time). Performance of the proposed formulation is clearly superior when using higher relaxation parameters, avoiding excessive computational effort and, in many cases, allowing for convergence to be achieved. However, the fully implicit method herein was beneficial to the numerical stability of the equation set when non-orthogonal meshes were employed. For orthogonal grids, Δx_η^e is of null value and terms of the non-linear fluxes, which are implicitly treated, are reduced in their numerical value (see Equation (80)). For orthogonal meshes, the gain in stability is not pronounced because only a small part of the first non-linear term contributes to diagonal dominance of the matrix of coefficients. Also observed was that the proposed implicit treatment only brought advantages to the robustness of the equation set when the high Reynolds formulation was used. For the low Reynolds number model, the use of damping functions and the need of a much finer grid always yielded convergence, and at the same rate, when both implicit and explicit handling of the non-linear diffusion terms were computed.

7. CONCLUSIONS

In this work a new numerical treatment was presented for linear and non-linear diffusion fluxes to avoid convergence difficulties. Improvements in the prediction of turbulent flows, where the normal Reynolds stresses play an important role, also were shown. The model that presented smaller deviations from the experimental data was the NL_LRN model. For the back-step case shown in Figure 4, all models reproduced reasonably well experimental values, with better predictions given by NL_LRN model within the range $0.5<Y/H<0.8$. With the NL_HRN closure, better performance was obtained for $0.7<Y/H<1.0$. Figures 5 and 7 show that the proposed implicit numerical treatment for non-linear diffusion fluxes enhances the numerical stability of the code,

DOI: 10.1002/fld

allowing for the use of higher relaxation parameters without solution divergence. Consequences are that numerical solution stability is achieved when compared to solving the same problem using the standard fully explicit formulation.

Ultimately, application of the implicit method described here showed that the stability of the solution either increases (high Reynolds with non-orthogonal mesh) or remains the same (low Reynolds number applications). Therefore, one of the disadvantages of the proposed method, when using in conjunction with LRN models, for the cases here analyzed, is that it produces solutions of comparable stability at expense of increasing the number of floating point operations, which is demanded by using a more complex non-linear stress–strain relationship. Nevertheless, the semi-implicit handling of non-linear terms described here, after fully tested in more complex and real world problems, may represents an alternative path when robust fluid flow solutions are sought for engineering flows of practical relevance and of general difficult convergence. Additional advantages of the procedure proposed here lie in the possibility of testing different non-linear expressions if one considers the enhanced robustness and stability obtained for the entire numerical algorithm. More complex constitutive equations may use the proposition described here for testing the calculations in more complex and computational demanding flows.

ACKNOWLEDGEMENTS

The authors thank CNPq, Brazil, for their financial support during the preparation of this work.

REFERENCES

1. de Lemos MJS. A block-implicit numerical procedure for simulation of buoyant swirling flows in a model furnace. *International Journal for Numerical Methods in Fluids* 2003; **43**(3):281–299.
2. Jones WP, Launder BE. The prediction of laminarization with two-equation model of turbulence. *Internatinal Journal of Heat and Mass Transfer* 1972; **15**:301–314.
3. Launder BE, Reece GJ, Rodi W. Progress in the development of a Reynolds stress turbulence closure. *The Journal of Fluid Mechanics* 1975; **68**:537.
4. Rodi W. The prediction of free turbulent boundary layers by use of a two-equation model of turbulence. *Ph.D. Thesis*, University of London, 1972.
5. de Lemos MJS, Sesonske A. Turbulence modeling in combined convection in liquid-metal pipe flow. *International Journal of Heat and Mass Transfer* 1985; **28**(6):1067–1088.
6. de Lemos MJS. Anisotropic turbulent transport modeling for Rod-Bundle. *International Journal of Heat and Technology* 1988; **6**(1–2):27–37.
7. Warsi ZUA, Amlicke B. Improved algebraic relation for the calculation of Reynolds stresses. *AIAA Journal* 1976; **14**:1779.
8. Rivlin RS. The relation between the flow of non-Newtonian fluids and turbulent Newtonian fluids. *Quarterly of Applied Mathematics* 1957; **15**:212.
9. Speziale CG. On nonlinear $k-1$ and $k-\varepsilon$ models of turbulence. *The Journal of Fluid Mechanics* 1987; **176**:459–475.
10. Lumley JL. Toward a turbulent constitutive relation. *The Journal of Fluid Mechanics* 1970; **41**:413.
11. Nisizima S, Yoshizawa A. Turbulent channel and Couette flows using an anisotropic $k-\varepsilon$ model. *AIAA Journal* 1987; **25**(3):414.
12. Rubinstein R, Barton JM. Renormalization group analysis of the stress transport equation. *Physics of Fluids* 1990; **A2**:1472.
13. Shih TH, Zhu J, Lumley JL. A realizable Reynolds stress algebraic equation model. *NASA TM-105993*, 1993.
14. Gatski TB, Speziale CG. On explicit algebraic stress models for complex turbulent flows. *The Journal of Fluid Mechanics* 1993; **254**:59–78.
15. Bauer W, Haag O, Hennecke DK. Accuracy and robustness of nonlinear eddy viscosity models. *International Journal of Heat and Fluid Flow* 2000; **21**:312–319.
16. Abid R, Rumsey C, Gatski TB. Prediction of nonequilibrium turbulent flows with explicit algebraic stress models. *AIAA Journal* 1995; **33**(11):2026–2031.
17. Rahman M, Rautaheimo P, Siikonen T. Numerical study of turbulent heat transfer from a confined impinging jet using a pseudo-compressibility method. In *Turbulence, Heat and Mass Transfer 2*, Hanjalic K, Peeters T (eds). Delf University Press: Delft, 1997; 511–520.
18. Launder BE, Spalding DB. The numerical computation of turbulent flows. *Computer Methods in Applied Mechanics and Engineering* 1974; **3**:269–289.
19. Abe K, Nagano Y, Kondoh T. An improved $k-\varepsilon$ model for prediction of turbulent flows with separation and reattachment. *Transactions of JSME, Series B* 1992; **58**:3003–3010.

DOI: 10.1002/fld

20. Pope SB. A more general effective-viscosity hypothesis. *The Journal of Fluid Mechanics* 1975; **72**:331.
21. Park TS, Sung HJ. A nonlinear low-Reynolds-number $k-\varepsilon$ model for turbulent separated and reattaching flows. *International Journal of Heat and Mass Transfer* 1995; **38**:2657–2666.
22. Pedras MHJ, de Lemos MJS. Simulation of turbulent flow in porous media using a spatially periodic array and a low Re two-equation closure. *Numerical Heat Transfer*, *Part A*: *Applications* 2001; **39**(1):35–59.
23. Khosla PK, Rubin SG. A diagonally dominant second-order accurate implicit scheme. *Computers and Fluids* 1974; **2**(12):207.
24. Patankar SV. *Numerical Heat Transfer and Fluid Flow*. Mc-Graw Hill: New York, 1980.
25. Assato M, de Lemos MJS. Development of a non-linear turbulence model for recirculating flows using generalized coordinates. *ENCIT98—Proceedings of the 7th Brazilian Congress of Engineering and Thermal Sciences*, vol. 2, Rio de Janeiro, RJ, 3–6 November 1998; 1386–1391.
26. de Lemos MJS. Flow and heat transfer in rectangular enclosures using a new block-implicit numerical method. *Numerical Heat Transfer*, *Part B*: *Fundamentals* 2000; **37**(4):489–508.
27. de Lemos MJS. A block-implicit method for numerical simulation of swirling flows in a model combustor. *International Communications in Heat And Mass Transfer* 2003; **30**(3):369–378.
28. Patankar SV, Spalding DB. A calculation procedure for heat, mass and momentum transfer in three-dimensional parabolic flows. *International Journal of Heat and Mass Transfer* 1972; **15**:1787–1806.
29. Stone HL. Iterative solution of implicit approximations of multi-dimensional partial differential equations. *SIAM Journal on Numerical Analysis* 1968; **5**:530–558.
30. Braga EJ, De Lemos MJS. Turbulent natural convection in a porous square cavity computed with a macroscopic $k-\varepsilon$ model. *International Journal of Heat and Mass Transfer* 2004; **47**(26):5639–5650.
31. Santos NB, de Lemos MJS. Flow and heat transfer in a parallel-plate channel with porous and solid baffles. *Numerical Heat Transfer*, *Part A*: *Applications* 2006; **49**:546–556.
32. Kim J, Kline SJ, Johnston JP. Investigation of a reattaching turbulent shear layer: flow over a backward-facing step. *ASME Journal of Fluids Engineering* 1980; **102**:302–308.
33. Heyerichs K, Pollard A. Heat transfer in separated and impinging turbulent flows. *International Journal of Heat and Mass Transfer* 1996; **39**(12):2385–2400.
34. Craft TJ, Launder BE, Suga K. Extending the applicability of eddy-viscosity models through the use of deformation invariants and non-linear elements. *Proceedings of the Fifth International Symposium on Refined Flow Modeling and Turbulence Measurements*, Paris, 1993.
35. Assato M, Pedras MHJ, de Lemos MJS. Numerical solution of turbulent channel flow past a backward-facing step with a porous insert using linear and nonlinear $k-\varepsilon$ models. *Journal of Porous Media* 2005; **8**(1):13–29.
36. Assato M, de Lemos MJS. Turbulent flow in wavy channels simulated with nonlinear models and a new implicit formulation. *Numerical Heat Transfer*, *Part A*: *Applications* 2009; **56**(4):301–324.

DOI: 10.1002/fld